

A shock-capturing meshless method for solving the one-dimensional Saint-Venant equations on a highly variable topography

D. Satyaprasad^a, Soumendra Nath Kuiry^{id}^{b,*} and S. Sundar^a

^a Centre for Computational Mathematics and Data Science, Department of Mathematics, Indian Institute of Technology Madras, Chennai, Tamil Nadu 600036, India

^b Department of Civil Engineering, Indian Institute of Technology Madras, Chennai, Tamil Nadu 600036, India

*Corresponding author. E-mail: snkuiry@civil.iitm.ac.in; snkuiry@gmail.com

 SNK, 0000-0001-6365-6849

ABSTRACT

The Saint-Venant equations are numerically solved to simulate free surface flows in one dimension. A Riemann solver is needed to compute the numerical flux for capturing shocks and flow discontinuities occurring in flow situations such as hydraulic jump, dam-break wave propagation, or bore wave propagation. A Riemann solver that captures shocks and flow discontinuities is not yet reported to be implemented within the framework of a meshless method for solving the Saint-Venant equations. Therefore, a wide range of free surface flow problems cannot be simulated by the available meshless methods. In this study, a shock-capturing meshless method is proposed for simulating one-dimensional (1D) flows on a highly variable topography. The Harten–Lax–van Leer Riemann solver is used for computing the convective flux in the proposed meshless method. Spatial derivatives in the Saint-Venant equations and the reconstruction of conservative variables for flux terms are computed using a weighted least square approximation. The proposed method is tested for various numerically challenging problems and laboratory experiments on different flow regimes. The proposed highly accurate shock-capturing meshless method has the potential to be extended to solve the two-dimensional (2D) shallow water equations without any mesh requirements.

Key words: Harten–Lax–van Leer Riemann solver, meshless method, Saint-Venant equations, shock-capture, weighted least square

HIGHLIGHTS

- A shock-capturing meshless method is presented for solving the 1D Saint-Venant equations on a highly variable topography.
- The points are irregularly distributed along the channel to define minute topographical features.
- The meshless method can accurately capture shocks and flow discontinuity in open channel flows.

INTRODUCTION

The free surface flow resulting from dam-break, levee breaching, or tidal bore propagation falls in the category of transcritical flow, wherein the flow regime changes from subcritical to supercritical and vice versa. The flow transition can be accurately described by a shock-capturing numerical scheme. Such flows may be treated as one-dimensional (1D) or two-dimensional (2D), depending on the flow dynamics and practical requirements. Although 2D flow models have gained tremendous popularity in the last two decades due to advancements in computing power and robust numerical schemes, 1D models are still in use for simulating flows dominant in one direction, especially for large computational domains. Moreover, the coupled 1D–2D models (Ghostine *et al.* 2015) are nowadays suitably used to reduce overall computation time and ensure enough lead time. This assists emergency action planning in cases of disasters such as dam-break flow, bore and flood wave propagation, and discontinuous flow (i.e., flows with shocks) that travels downstream of hydraulic structures. The Saint-Venant equations (i.e., shallow water equations in unidirectional form) are numerically solved to simulate 1D flows with discontinuity and shocks. Several numerical schemes have been developed for solving the Saint-Venant equations, such as the finite difference method (FDM) (Fennema & Chaudhry 1990; Molls & Chaudhry 1995), the finite element method (FEM) (Liang *et al.* 2008) and the finite volume method (FVM) (Eymard *et al.* 2000; LeVeque 2002; Yoon & Kang 2004; George 2008; Kuiry *et al.* 2008; Haleem *et al.* 2015). However, meshless methods, alias gridless or meshfree, or particle methods, are also

This is an Open Access article distributed under the terms of the Creative Commons Attribution Licence (CC BY 4.0), which permits copying, adaptation and redistribution, provided the original work is properly cited (<http://creativecommons.org/licenses/by/4.0/>).

becoming increasingly popular in recent years for simulating fluid flow problems. Several meshless methods have been developed, such as the smoothed particle hydrodynamics (SPH) (Gingold & Monaghan 1977), the finite pointset method (FPM) (Tiwari & Kuhnert 2003a, 2003b), the element-free Galerkin (EFG) method (Belytschko *et al.* 1995), the generalized finite difference method (GFDM) (Li & Fan 2017), and the discrete mixed subdomain least squares method (Fazli Malidareh *et al.* 2016). However, meshless methods are relatively new to free surface flow simulations. In particular, shock-capturing meshless methods for simulating flows with shocks and discontinuity are scarce in the literature.

The oldest and the most popularly used mesh-free method is the SPH. Although SPH was initially developed for astrophysical fluid dynamics (Gingold & Monaghan 1977), it was later extended to hydrodynamic modeling by Monaghan (1992) for solving the Navier–Stokes equations for incompressible free surface flows. The numerical solution of 1D shallow water equations for open channel flow by SPH was described by Chang *et al.* (2011). The main difficulty of the SPH is the incorporation of boundary conditions, which are necessary for solving the Saint-Venant equations that describe real-world flow dynamics. However, the latest modification of the SPH method for shallow water equations by Vacondio *et al.* (2012a, 2012b, 2013) can deal with capturing shocks, open boundaries, and balancing discontinuous bed slopes. Later, the EFG method was proposed by Belytschko *et al.* (1995). This method came into existence as an extension of the diffuse element method proposed by Nayroles *et al.* (1992). In the EFG method, the generalized moving least square interpolation was used to define the local approximation of spatial derivatives. The FPM developed by Tiwari & Kuhnert (2003a) is extensively applied to various problems of fluid dynamics (Tiwari *et al.* 2007; Tiwari & Kuhnert 2002, 2007; Kuhnert 2003; Kuhnert & Ostermann 2014; Jefferies *et al.* 2015; Suchde *et al.* 2017). The FPM uses a weighted least square (WLS) method to approximate spatial derivatives at each point of the domain. The FPM is a Lagrangian model for fluid problems involving rapidly changing flow domains with respect to time (Tiwari & Kuhnert 2003a; Jefferies *et al.* 2015). In addition, it is relatively simple to implement and set the boundary conditions (Tiwari & Kuhnert 2003a).

Wang & Shen (1999) were the first to develop a meshless 1D shallow water model for the dam-break problem over a wet bed but without the source terms such as bed and friction slopes. As a result, the model application is limited to ideal shallow water flow problems. The presence of source terms creates a numerical imbalance between the driving forces (e.g., source terms) and convective fluxes and artificially accelerates the flow as the solution advances with time. The study by Rogers *et al.* (2003) illustrated that such imbalance is created when different terms are discretized using different methods. Therefore, a consistent discretization method is required to avoid artificial acceleration of the flow. Nevertheless, some notable meshless shallow water solvers such as GFDM by Li & Fan (2017), finite point method by Buachart *et al.* (2014) and radial basis function (RBF) by Chaabelasri (2018) are developed over time. However, the GFDM for shallow water equations results in wiggles near the discontinuities, especially for the 1D dam-break problems, as reported by Li & Fan (2017). The finite point method for shallow water equations by Buachart *et al.* (2014) has difficulties in handling complex source terms. The RBF-based meshless method for solving the shallow water equations uses artificial viscosity to capture shocks (Chaabelasri 2018). On the other hand, the FVM-based discretization for the Saint-Venant equations uses the Riemann solvers to accurately capture shocks and flow discontinuity without the need for artificial viscosity. Therefore, Riemann solvers may be incorporated within the framework of meshless methods to enhance their capability to capture physical features of shallow water flow dynamics such as discontinuities, shocks, abrupt variations in the bed topography, and flow variables (e.g., depth and velocity). The extensive literature review by the authors suggests that enough studies have not been carried out in the direction of using Riemann solvers in meshless methods. This is especially missing for simulating flows on highly variable topography using the meshless method. Hence, implementation of, for example, the Harten–Lax–van Leer (HLL) Riemann solver proposed by Harten *et al.* (1983) with a two-wave model resolving three constant states can enhance the capability of meshless methods to solve practical shallow water flow problems.

The numerical solution of the shallow water equations for domains like rivers and prismatic channels does not need to change the domain geometry rapidly. Due to the nature of its relatively stable geometry, a meshless method that can represent the geometry by a fixed number of irregularly distributed points at the beginning, but need not be maintained later, may be adopted for solving the shallow water or the Saint-Venant equations. In this regard, the FPM is proven to be a robust method for complex fluid flow problems (Uhlmann *et al.* 2013; Tiwari *et al.* 2007; Jefferies *et al.* 2015). The FPM already serves as a numerical basis for two commercially used meshfree simulation tools, NOGRID by Moller & Kuhnert (2007) and VPS-PAM-CRASH by Tramecon & Kuhnert (2013). Due to the Lagrangian nature, the FPM is suitable for handling flow problems with complicated and even rapidly changing geometry with time. However, in FPM, the points move with physical properties such as mass, momentum, and velocity. Hence, in every few time steps, the points need to be managed through the neighbor

searching algorithm. Also, a few points need to be removed if the points get clustered in one place. On the other hand, new points need to be introduced if holes are found in the computational domain. Therefore, FPM needs to be implemented in the Eulerian framework to represent the geometry by a fixed number of irregularly distributed points at the beginning that need not be maintained later during the simulation. Such modification is required, especially for simulating flows on rigid bed topography. However, there is a lack of research on modeling the Saint-Venant equations using the Riemann solver-based meshfree method.

To fill this gap, in this study, we have developed a shock-capturing meshless method for solving the 1D Saint-Venant equations for simulating flows in nonprismatic open channels with abrupt variation in topography. The HLL approximate Riemann solver is implemented within the framework of a meshless method for capturing shocks and discontinuity. The proposed numerical scheme is well balanced due to the adoption of the Saint-Venant equations in the form given by Ying & Wang (2008), which automatically incorporates the surface gradient method (SGM) of Zhou *et al.* (2001). The physical domain is represented by a set of irregularly distributed points. A local cloud of neighboring points, called satellites, is identified for each of these points. Local approximations for the spatial derivatives are performed by using the WLS method. In the WLS method, the weight function can be quite arbitrary, but in our computations, a Gaussian weight function, as described in the FPM method by Tiwari & Kuhnert (2003b), is considered. The water surface gradient in the source term is treated as the average water surface level at the midpoints of the center and satellite points of the local cloud by using the piece-wise linearly reconstructed variables. The driving forces and fluxes are also computed using the piece-wise linearly reconstructed variables. This ensures that the solution scheme is consistent and well balanced. The HLL Riemann solver and consistent discretization enable the proposed meshless method to effectively handle discontinuous and shock flows on a variable bed topography. The performance of the proposed meshfree method is verified by solving various analytical test cases, including water at rest condition over an irregular bed and variable width, dam-break flow on a wet and dry horizontal bed, steady flow over a hump with a hydraulic jump, dam-break flow over a hump, and tidal flow over a vertical step. The proposed meshless method is then validated by simulating laboratory experiments on hydraulic jump in a diverging channel and dam-break wave propagation over a triangular hump. The results show that the proposed method is highly accurate and does not diffuse at the wavefront. The developed meshless method with the HLL approximate Riemann solver eliminates the formation of wiggles at the wavefront and accurately handles the complex source terms, unlike the existing meshless methods (e.g., GFDM and FPM) (Buachart *et al.* 2014; Li & Fan 2017). Moreover, the proposed meshless method does not require any artificial viscosity to dampen numerical oscillations observed in earlier implementations (e.g., Chabelasri 2018). Thus, the novelty of the study is to successfully implement the shock-capturing scheme within the meshless method and analyze its accuracy. It should be noted that the true advantages of a meshless method can be realized in 2D applications. In that context, the present study can be considered as a foundation for advancing research on the implementation of the proposed meshless shock-capturing method for solving the 2D shallow water equations for real-world problems and thereby realizing its full advantages.

GOVERNING EQUATIONS

The 1D Saint-Venant equations for unsteady flow in a channel with irregular cross-sections can be written in the following conservative form as given in Ying *et al.* (2004):

$$\frac{\partial \mathbf{U}}{\partial t} + \frac{\partial \mathbf{F}(\mathbf{U})}{\partial x} = \mathbf{S}(\mathbf{U}) \quad (1)$$

Where \mathbf{U} is the vector of conservative variables, $\mathbf{F}(\mathbf{U})$ are the fluxes and $\mathbf{S}(\mathbf{U})$ are the source terms defined as

$$\mathbf{U} = \begin{bmatrix} A \\ Q \end{bmatrix}, \quad \mathbf{F}(\mathbf{U}) = \begin{bmatrix} Q \\ \frac{Q^2}{A} \end{bmatrix}, \quad \mathbf{S} = \begin{bmatrix} 0 \\ -gA \frac{\partial Z}{\partial x} - g \frac{n^2 Q |Q|}{R^{4/3} A} \end{bmatrix}$$

where A is the cross-sectional area and a function of flow depth h , Q is the flow rate or discharge, g is the gravitational acceleration, $Z = z + h$ is the water surface level from a datum as shown in Figure 1; in which z is the bottom topography, n denotes the Manning coefficient, $R = A/P$ is the hydraulic radius; in which P is the wetted perimeter of the channel. In Figure 1, B is the top width of the flow through the cross-section.

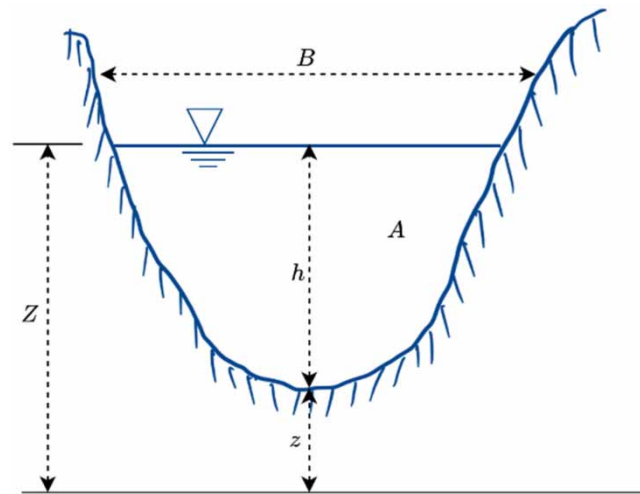


Figure 1 | Definition sketch of the cross-section.

Ying *et al.* (2004) argued that the above form of the Saint-Venant equations (Equation (1)) is common in engineering practice for finding out the required flow variables h and Q . In the other form of the equations, the surface gradient dZ/dx is split into hydrostatic pressure and bed slope source terms. Rogers *et al.* (2003) observed that the simulated flow artificially accelerates in the case of still-water conditions due to different discretization methods for the split terms. Zhou *et al.* (2001) proposed the SGM and pointed out that the main source of error is caused by inaccurate reconstruction of water depth. Therefore, in this study, the driving forces are taken into a single term (i.e., water surface gradient) in Equation (1), so it avoids the numerical imbalance and results in a well-balanced scheme, as discussed in the following section.

NUMERICAL METHOD

The meshless method based on FPM is proposed in this study to solve the 1D Saint-Venant equations. The physical domain is represented by a set of an irregularly distributed finite number of points, which possess fluid properties such as depth, velocity, and momentum. For each of these points, a local cloud of neighboring points is identified. The cloud points around the considered point are called satellites. Local approximations of the spatial derivatives are performed using the WLS method. The standard FPM (Tiwari & Kuhnert 2003b) is Lagrangian in nature, and points move with fluid properties along the flow domain. Due to its Lagrangian nature, the FPM is suitable for handling flow problems with complicated and even rapidly changing geometry with time. However, for every few time steps, the points need to be managed through a neighbor searching algorithm so that points can be removed if they are clustered in one place or filled with new points if holes appear during the simulation.

In this study, due to the nature of rigid bed geometry in open channel flows, we have adopted the FPM but in the Eulerian framework for solving the 1D Saint-Venant equations (Equation (1)). In the proposed method, the points distributed at the beginning need not be maintained later during the simulation. The convective flux term is computed using the HLL Riemann solver to simulate the discontinuous flow. Therefore, using the HLL Riemann solver within the meshless method is a major contribution of this study. The source terms are also considered for solving real-world problems. The numerical imbalance between bed slope and convective flux terms is avoided following the SGM of Zhou *et al.* (2001). The well-balanced and shock-capturing meshless method is presented below.

Least square approximation of derivatives

In many practical applications, the mesh-based numerical schemes, such as FDM, FEM, and FVM, play a very important role in determining the accuracy of a numerical solution. However, they may lose accuracy if the grid points are poorly distributed. The method presented herein does not require regular grids to approximate spatial derivatives of a function because the proposed meshless method uses the cloud of grid points instead of neighboring grid points alone. In this section, we present the basic theory of the WLS method to approximate spatial derivatives of a function.

Let $\Omega = [a, b] \subset R$ be a domain containing N number of scattered points and $f:\Omega \rightarrow R$ be a scalar function and $f(x_i)$ be its discrete values at the points $x_i \in \Omega$ for $i = 1, 2, \dots, N$. Figure 2 shows an example of the typical distribution of points in the domain. These points are numerical grid points x_i . The neighboring cloud of points C_i for the i th grid point are considered as shown in Figure 3. In the cloud, the considered point x_i is the center, and the other points are called the satellites. Let M_i be the total number of satellites in the cloud C_i .

The coordinate difference between the satellite x_j and the center x_i can be expressed as

$$\Delta x_i^j = x_j - x_i \tag{2}$$

Let the vector $\vec{r}_i^j = \Delta x_i^j$ start from x_i to x_j , and its length is given by

$$r_i^j = |\Delta x_i^j| \tag{3}$$

and the reference length of the cloud is

$$L_i = \max_{x_j \in C_i} r_i^j \tag{4}$$

To approximate the spatial derivatives of the function f at some point x_i based on the discrete values of its neighboring points, a WLS method (Tiwari & Kuhnert 2003b) is adopted in the present work like the earlier studies of meshfree methods (Tiwari & Kuhnert 2003a; Ma et al. 2008). The weight function can be quite arbitrary; however, we consider a Gaussian weight function of the form:

$$w(x_i - x; L_i) = \begin{cases} \exp\left(-\alpha \frac{|x_i - x|^2}{L_i^2}\right), & \text{if } \frac{|x_i - x|}{L_i} \leq 1 \\ 0, & \text{otherwise} \end{cases} \tag{5}$$

where α is a positive constant and is considered as 6.25 in our numerical computations as it gives the best approximation of derivatives. The derivatives of the function f at the point x_i are determined using the Taylor series about the point x_i and can be expressed in the following form:

$$f(x) = f(x_i) + \left(\frac{\partial f}{\partial x}\right)_i (x - x_i) + \frac{1}{2} (x - x_i)^2 \left(\frac{\partial^2 f}{\partial x^2}\right)_i + O(k^3) \tag{6}$$

where $k = x - x_i$.



Figure 2 | A typical distribution of points in the domain Ω .

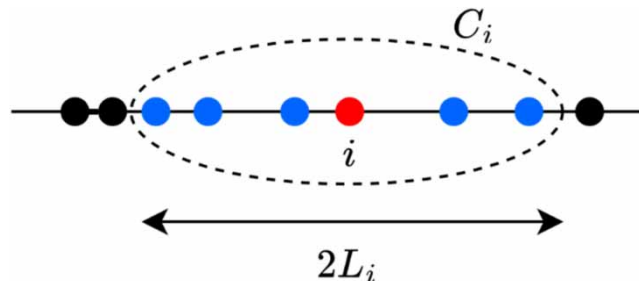


Figure 3 | A typical meshless cloud of points.

As the Saint-Venant equations have only first-order partial derivatives, it is reasonable enough to maintain up to first-order terms in Equation (6). Hence, the approximate value is expressed as

$$\tilde{f}(x_j) = f(x_j) + \left(\frac{\partial f}{\partial x}\right)_i (x_j - x_i) \quad (7)$$

and the error between the exact and approximate values can be written as

$$e_j = f(x_j) - \tilde{f}(x_j) = f(x_j) - \left(f(x_i) + \left(\frac{\partial f}{\partial x}\right)_i (x_j - x_i)\right) = f(x_j) - f(x_i) - a(x_j - x_i) \quad (8)$$

The spatial derivative $a = \left(\frac{\partial f}{\partial x}\right)_i$ in Equation (8) can be computed by minimizing the following norm over the neighboring cloud C_i

$$\Phi = \sum_{j=1}^{M_i} w_j e_j^2 \quad (9)$$

and the minimization of Φ is given by $\frac{\partial \Phi}{\partial a} = 0$. This yields

$$a = \sum_{j=1}^{M_i} \alpha_j (f_j - f_i) \quad (10)$$

where

$$\alpha_j = \frac{w_j (x_j - x_i)}{\sum_{j=1}^{M_i} w_j (x_j - x_i)^2} \quad (11)$$

Alternatively, the spatial derivative $a = \left(\frac{\partial f}{\partial x}\right)_i$ can also be estimated using the midpoint between i and j as

$$a = \left(\frac{\partial f}{\partial x}\right)_i = \sum_{j=1}^{M_i} \alpha_{ij} (f_{ij} - f_i) \quad (12)$$

where $\alpha_{ij} = 2\alpha_j$ and f_{ij} is estimated at the midpoint between i and j (Chen & Shu 2005; Ma *et al.* 2008).

Generating grid points

The grid points may cluster or scatter if they are generated randomly. To avoid this, we consider two parameters λ and μ such that $0 < \lambda < \mu < 1$. The algorithm starts with initializing the boundary points. Then, the first interior point is filled having a minimal distance $\lambda \Delta x$ and a maximal distance $\mu \Delta x$ from the current point, where Δx is the average distance between the points. The same procedure is followed until the entire domain is filled with grid points. In our numerical computations, we set the values as $\lambda = 1/3$ and $\mu = 2/3$.

Spatial discretization

The spatial derivatives in the flux terms of Equation (1) are needed for every cloud point. Equation (12) is applied for spatial discretization of the flux terms and the following expression is obtained:

$$\left(\frac{\partial \mathbf{U}}{\partial t}\right)_{C_i} + \left(\frac{\partial \mathbf{F}}{\partial x}\right)_{C_i} = (\mathbf{S})_{C_i} \quad (13)$$

For simplicity, we use the subscript i to represent the cloud C_i and substitution of Equation (12) into Equation (13) results in

$$\frac{\partial \mathbf{U}_i}{\partial t} + \sum_{j=1}^{M_i} \alpha_{ij} (\mathbf{F}_{ij} - \mathbf{F}_i) = \mathbf{S}_i \quad (14)$$

The flux function \mathbf{F} through the midpoint of ij is evaluated by the two states on the left (\mathbf{U}^L) and right (\mathbf{U}^R) of the midpoint

$$\mathbf{F}_{ij} = \mathbf{F}(\mathbf{U}_{ij}^L, \mathbf{U}_{ij}^R) \quad (15)$$

If $\mathbf{U}_{ij}^L = \mathbf{U}^L$ and $\mathbf{U}_{ij}^R = \mathbf{U}^R$ are chosen for computing the flux through the midpoint using Equation (15) instead of just at the left (i.e., \mathbf{U}_{ij}^L) and right (i.e., \mathbf{U}_{ij}^R) of the midpoint (i.e., where the discontinuity is assumed to exist), the numerical scheme results in a first-order numerical scheme, which is often diffusive in nature. For higher order spatial accuracy, the variables are reconstructed at the midpoint. Since Z and B are also required to be defined at the midpoint, like the variables A and Q , they all are reconstructed in the same way. For this purpose, we define the vector, $\mathbf{W} = (A, Q, Z, B)$ and the left and right states are reconstructed as

$$\mathbf{W}_{ij}^L = \mathbf{W}_i + \frac{1}{2} \nabla \mathbf{W}_i \cdot \mathbf{r}_i^j \quad (16.a)$$

$$\mathbf{W}_{ij}^R = \mathbf{W}_j - \frac{1}{2} \nabla \mathbf{W}_j \cdot \mathbf{r}_i^j \quad (16.b)$$

where $\nabla \mathbf{W}_i = \left(\frac{\partial \mathbf{W}}{\partial x} \right)_i$

The reconstruction by Equation (16) often results in local *maxima* or *minima*. As a consequence, unphysical oscillations appear and propagate in the computational domain, spoiling the numerical solution. In order to limit the gradients for the reconstruction of variables, a nonlinear function, known as *limiter*, is used. The *minmod* slope limiter is used here for its easy implementation and ability to eliminate under or overshoots in the reconstructed variables (Zhou *et al.* 2001). The *minmod* slope limiter is estimated about the cloud C_i using the WLS method as follows:

$$\left(\frac{\partial \mathbf{W}}{\partial x} \right)_i = \text{minmod} \left(\left. \frac{\partial \mathbf{W}}{\partial x} \right|_{C_i^L}, \left. \frac{\partial \mathbf{W}}{\partial x} \right|_{C_i^R} \right) \quad (17)$$

$$\left. \frac{\partial \mathbf{W}}{\partial x} \right|_{C_i^L, C_i^R} = \sum_{j \in C_i^L, C_i^R} \alpha_j (\mathbf{W}_j - \mathbf{W}_i) \quad (18)$$

where C_i^L and C_i^R are left- and right-side points of the center of the cloud C_i .

The HLL approximate Riemann solver

The HLL approximate Riemann solver proposed by Harten *et al.* (1983) is used to calculate the midpoint flux \mathbf{F}_{ij} , because of its robustness and ease of implementation. The approximate solution may be expressed by the three averaged states as

$$\mathbf{U}_{ij} = \begin{cases} \mathbf{U}_{ij}^L & \text{if } S_L \geq 0 \\ \mathbf{U}_{ij}^* & \text{if } S_L < 0 < S_R \\ \mathbf{U}_{ij}^R & \text{if } S_R \leq 0 \end{cases} \quad (19)$$

where S_L and S_R define the left and right wave speeds of the two states and are given by

$$S_L = \min\left(u_L - \sqrt{g\bar{h}_L}, u^* - \sqrt{gh^*}\right) \quad (20.a)$$

$$S_R = \min\left(u_R + \sqrt{g\bar{h}_R}, u^* - \sqrt{gh^*}\right) \quad (20.b)$$

where u_L and u_R are velocities of the left and right states, respectively, and the variables at the intermediate state are defined as

$$u^* = \frac{1}{2}(u_L + u_R) + \sqrt{g\bar{h}_L} - \sqrt{g\bar{h}_R} \quad (21)$$

$$\sqrt{gh^*} = \frac{1}{2}\left(\sqrt{g\bar{h}_L} + \sqrt{g\bar{h}_R}\right) + \frac{1}{4}(u_L - u_R) \quad (22)$$

where u^* and h^* are the velocity and flow depth of the intermediate state, and \bar{h}_L and \bar{h}_R are the averaged water depths ($\bar{h} = A/B$) of the left and right states.

The midpoint flux is now defined as

$$F(\mathbf{U}_{ij}^L, \mathbf{U}_{ij}^R) = \begin{cases} \mathbf{F}_{ij}^L & \text{if } S_L \geq 0 \\ \mathbf{F}_{ij}^* & \text{if } S_L < 0 < S_R \\ \mathbf{F}_{ij}^R & \text{if } S_R \leq 0 \end{cases} \quad (23)$$

In the case of channels with irregular cross-sections, the flux $\mathbf{F}_{ij}^* = [f_1^*, f_2^*]^T$ at the intermediate state is computed as described by Ying & Wang (2008), given by

$$f_1^* = \frac{S_R B_R f_1^L - S_L B_L f_1^R + S_L B_L S_R B_R (Z_R - Z_L)}{S_R B_R - S_L B_L} \quad (24.a)$$

$$f_2^* = \frac{S_R f_2^L - S_L f_2^R + S_L S_R (Q_R - Q_L)}{S_R - S_L} \quad (24.b)$$

where f_1 and f_2 are two components of the flux \mathbf{F} , that is $[f_1, f_2]^T = [Q, Q^2/A]^T$.

However, the wave propagation over a dry bed is a special case. For that, the wave speeds S_L and S_R are estimated according to the following expressions:

$$S_L = u_L - \sqrt{g\bar{h}_L}, \quad S_R = u_L + 2\sqrt{g\bar{h}_L} \quad \text{for right dry bed} \quad (25)$$

$$S_L = u_R - 2\sqrt{g\bar{h}_R}, \quad S_R = u_L + \sqrt{g\bar{h}_R} \quad \text{for left dry bed} \quad (26)$$

Source terms

The source terms in the momentum equation (i.e., Equation (1)) need to be properly estimated in order to construct a stable and well-balanced scheme. This can be achieved by treating the water surface gradient in the same way as the fluxes are treated using the piece-wise linearly reconstructed variables. The water surface gradient is then estimated as

$$\left(\frac{\partial z}{\partial x}\right)_{C_i} = \sum_{j=1}^{M_i} \alpha_{ij}(\bar{z}_{ij} - z_i) \quad (27)$$

where $\bar{z}_{ij} = (z_{ij}^L + z_{ij}^R)/2$ is the average water surface level at the midpoint.

It is important to note that Equation (27) relates the water surface gradient to the piece-wise linearly reconstructed water surface level. This makes the numerical scheme consistent and well balanced, and artificial acceleration of flow is eliminated (Ying & Wang 2008).

The friction source term is explicitly evaluated in each cloud C_i using the averaged values of flow variables Q and A over the cloud C_i .

Stability criteria

The current numerical scheme is explicit in nature and its stability is controlled by the Courant–Friedrichs–Lewy (CFL) condition. In the absence of a suitable stability condition for explicit meshless methods, the present study uses the CFL condition (Equation (28)) for calculating an appropriate stable time step Δt at the start of each time step:

$$\Delta t = C_{CFL} \min_{1 \leq i \leq N} \left(\frac{L_i}{|u_i| + \sqrt{\frac{gA_i}{B_i}}} \right) \quad (28)$$

where C_{CFL} is the Courant number ($0 < C_{CFL} \leq 1$). In this study, $C_{CFL} = 0.5$ is used for all the test cases for obtaining convergent solutions.

Boundary conditions

The proposed meshless method is designed to work according to the flow regime at the boundaries. At boundaries, we introduce new points outside the actual flow domain as shown in Figure 4. In this method, we do not use any special treatment for the boundaries, simply include the new points along with the flow domain into the algorithm to update the flow variables at the boundaries. In an inflow subcritical boundary condition, discharge is specified at the new points and water surface level is evaluated by the WLS method as it does to the interior points. Similarly, for outflow subcritical boundary condition, water surface level is defined at new points and discharge is evaluated naturally by the algorithm. If the inflow is supercritical, both discharge and water level are specified at the upstream new points.

Temporal discretization

The governing equation (i.e., Equation (1)) is converted into spatially discretized form as in Equation (14) for numerical solution. After the discretization of fluxes in Equation (23) and water surface gradient in source terms in Equation (27), we can obtain the following equation:

$$\frac{\partial \mathbf{U}}{\partial t} = \mathbf{R} \quad (29)$$

where

$$\mathbf{R} = \mathbf{S}(\mathbf{U}) - \frac{\partial \mathbf{F}(\mathbf{U})}{\partial x}$$

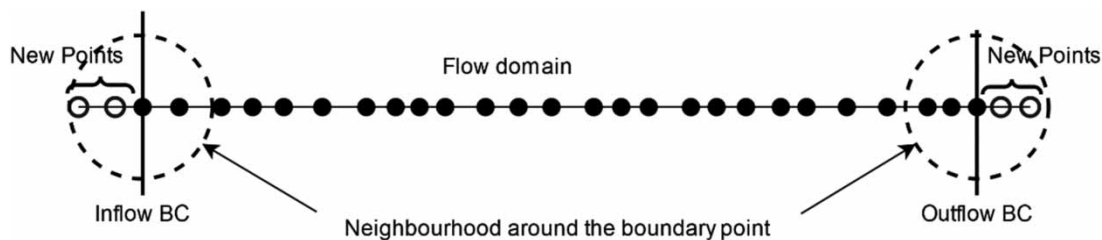


Figure 4 | Boundary at inflow and outflow; new points introduced at both boundaries.

Equation (14) can now be solved explicitly using the forward Euler time discretization for every cloud C_i . The forward discretization of Equation (29) is written as

$$\frac{U^{n+1} - U^n}{\Delta t} = R_i \quad (30)$$

where n and $n + 1$ denote the physical quantities at the n th and $(n + 1)$ th time steps. Therefore, the vector of conservative variables at $(n + 1)$ th time step can be obtained by

$$U_i^{n+1} = U_i^n + (\Delta t)R_i$$

A second-order Runge–Kutta time discretization was also implemented. However, the second-order time discretization did not show any noticeable difference in the results for the cases presented in the following section. On the contrary, the computation time was found to be significantly longer than the Euler time discretization. Therefore, the simple explicit time discretization described above is implemented in this study.

RESULTS AND DISCUSSION

The proposed meshless method for solving the 1D Saint-Venant equations is tested rigorously to examine its accuracy for various flow conditions. The problems are selected on subcritical, supercritical, transcritical flows, flows with shocks and discontinuity, variable width channels, and wave propagation on a dry bed, as discussed below.

Water at rest over an irregular bed and variable width

The conservation property of a numerical method can be badly affected when the source term of variable bed topography is not properly treated. In such cases, numerical methods can generate considerable oscillations and artificially accelerate the flow. The steady-state still-water condition on a variable bed topography is a standard test to examine the conservation property of a numerical scheme. We consider a quiescent steady-state case which was proposed by Goutal & Maurel (1997) to verify the ability of the proposed meshless method to maintain quiescent flow. The frictionless channel of length 1,500 m with variable width given in Table 1 and bed topography given in Table 2 are considered as the flow domain as shown in Figure 5.

The channel is represented by 250 irregularly distributed points. A zoomed-in view of a small length of the channel can be seen in Figure 6 for the distribution grid points. The simulation is continued for a long time, 1,000 s, until a steady state is achieved. The maximum error on water surface level and velocity in the channel are reported in Figure 6. It can be observed that the proposed meshless method can exactly maintain the quiescent condition throughout the domain with the difference in the order of 10^{-16} m/s for velocity and maximum deviation error is zero for water surface elevation, which are nothing but

Table 1 | Bed elevation (in meters)

x	0	50	100	150	250	300	350	400	425	435	450	475	500	505
$z(x)$	0	0	2.5	5	5	3	5	5	7.5	8	9	9	9.1	9
x	530	550	565	575	600	650	700	750	800	820	900	950	1,000	1,500
$z(x)$	9	6	5.5	5.5	5	4	3	3	2.3	2	1.2	0.4	0	0

Table 2 | Width of the channel (in meters)

x	0	50	100	150	200	250	300	350	400	425	435	450	470	475	500
$B(x)$	40	40	30	30	30	30	30	25	25	30	35	35	40	40	40
x	505	530	550	565	575	600	650	700	750	800	820	900	950	1,000	1,500
$B(x)$	45	45	50	45	40	40	30	40	40	5	40	35	25	40	40

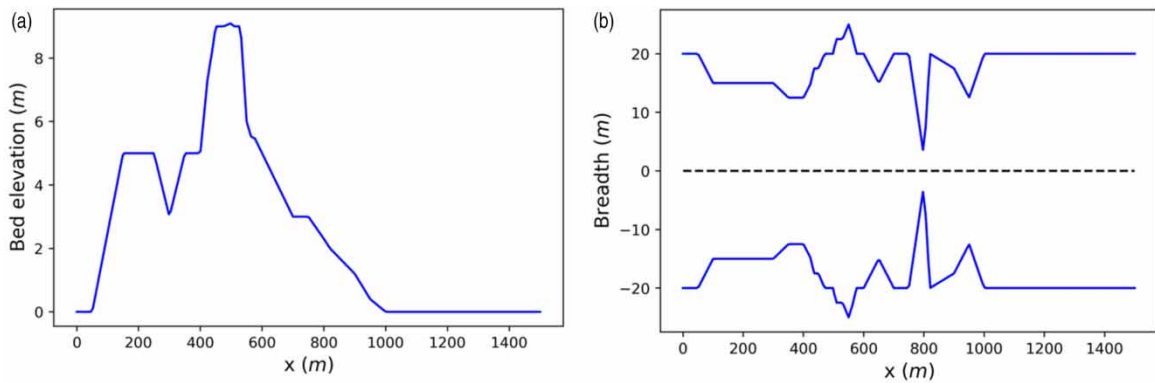


Figure 5 | Water at rest over an irregular bed and variable breadth: (a) bed topography and (b) channel breadth.

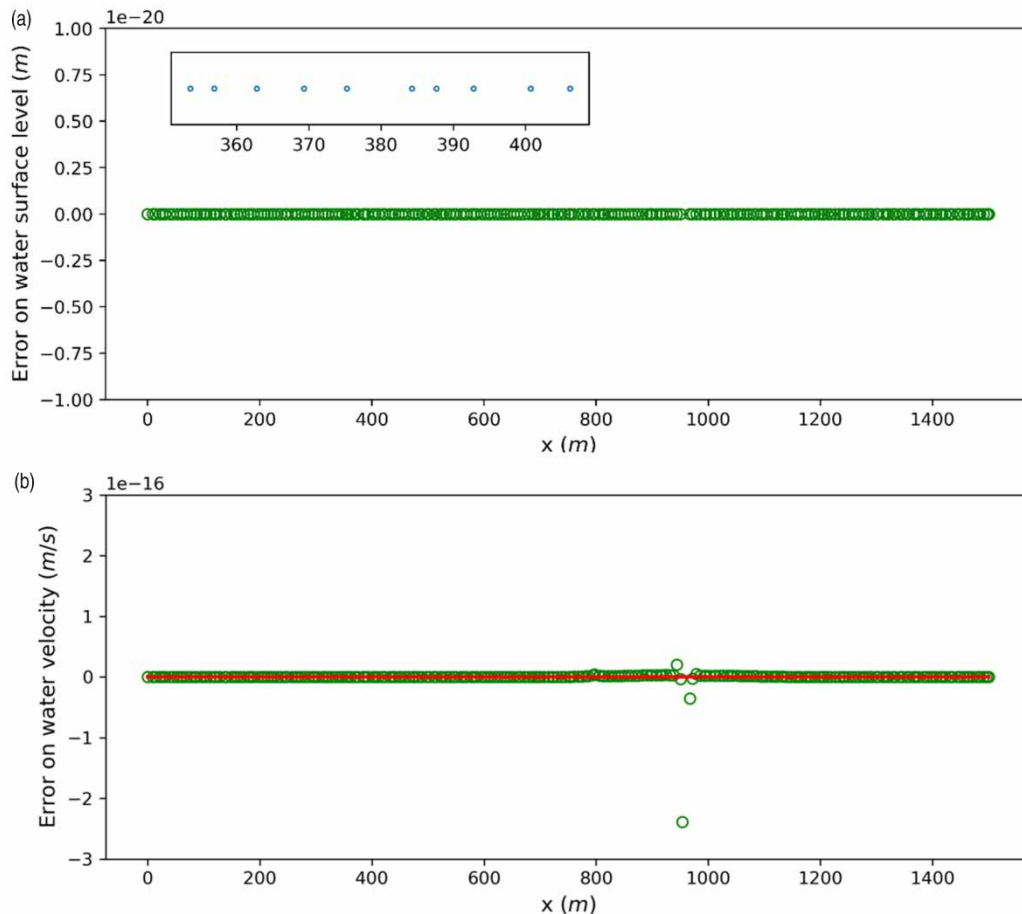


Figure 6 | Water at rest over an irregular bed and variable breadth: (a) water surface level and (b) discharge at time $t = 1000$.

the precision level of the computer. This confirms that the proposed meshless method maintains excellent balance between flux and source terms under the quiescent flow condition.

Again, the test is conducted on different number of equally spaced points and the maximum error of the water surface and velocity are recorded. The L_∞ error is defined as given below:

$$L_\infty(Z) = \max(Z - Z^e), \quad L_\infty(u) = \max(u - u^e)$$

The errors for different number of grid points are summarized in Table 3.

Dam break on wet and dry beds

This test case aims to study the ability of the model to simulate discontinuous flow and propagation of waterfront over wet and dry beds. A horizontal 1,200 m long rectangular channel with a frictionless bed is considered. A dam is located at $x = 500$ m from the upstream end. The initial upstream water depth is 10 m, and downstream water depth is 5 m for wet and 0 m for dry beds. A total of 600 meshless points are irregularly distributed along the channel length. At time $t = 0$ s, the dam is removed instantaneously. In the numerical computation, a dry bed tolerance of $h_{tol} = 0.000001$ m is used to distinguish between wet and dry bed, as discussed in Kuiry *et al.* (2012). The results are reported at 30 s after the removal of the dam. The computed water surface profiles and discharges compared with the analytical solutions are available in Toro (2001). Figures 7 and 8 show the wet bed and dry bed cases, respectively. It should be noted that the proposed meshless method can accurately capture the sharp changes in depth and velocity profiles, unlike the reported mesh-based finite volume solutions of Kuiry *et al.* (2012). Therefore, the proposed meshless model can accurately capture discontinuous flow with shocks over wet and dry beds.

For these two test cases, the effect of the minmod limiter is examined using four different meshless points $N = 80, 150, 300,$ and 600 . The nondimensional L_2 error norm of h and u for wet bed case and root mean square error of h and Q for wet bed are investigated. The error functions are defined as

$$L_2(h) = \sqrt{\frac{1}{N} \sum_{i=1}^N \left(\frac{h_i - h_i^e}{h_i^e} \right)^2} \quad L_2(u) = \sqrt{\frac{1}{N} \sum_{i=1}^N \left(\frac{u_i - u_i^e}{\sqrt{gh_i^e}} \right)^2}$$

$$h_{RMSE} = \sqrt{\frac{1}{N} \sum_{i=1}^N (h_i - h_i^e)^2}, \quad Q_{RMSE} = \sqrt{\frac{1}{N} \sum_{i=1}^N (q_i - q_i^e)^2}$$

Table 3 | The L_∞ errors in the computed water surface elevation and velocity on three different points

N	Maximum error for Z and u	
	$L_\infty(Z)$	$L_\infty(u)$
100	0	3.99×10^{-16}
200	0	2.01×10^{-16}
500	0	6.62×10^{-18}

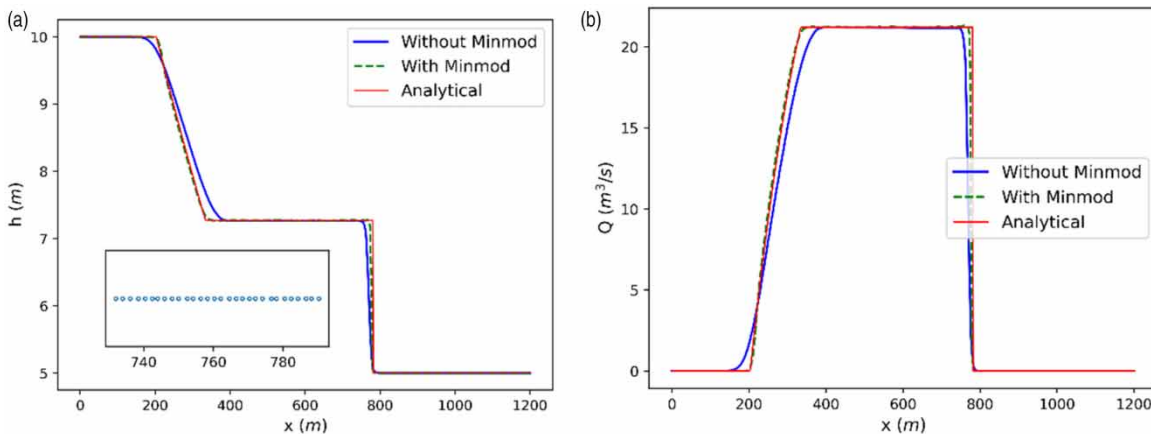


Figure 7 | Dam break on the wet bed: (a) water depth and (b) discharge.

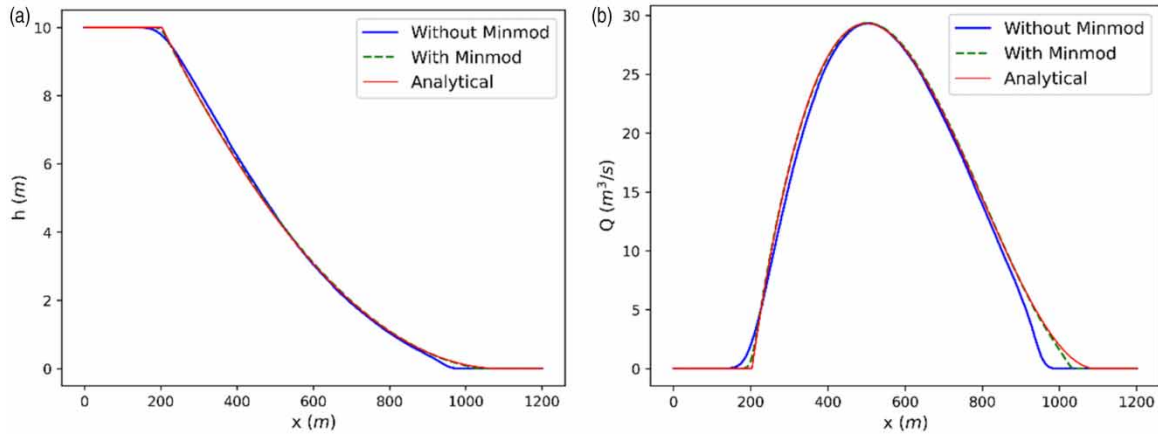


Figure 8 | Dam break on the dry bed: (a) water surface elevation and (b) discharge.

where N is total number of points in the domain; h_i and h_i^e are numerical and analytical values of the i th point; and u_i and u_i^e are the numerical and analytical values of the i th point. Tables 4 and 5 summarize the errors for different values of N .

Dam break flow on a variable bottom topography

The previous test cases do not consider the bed variation. However, in this test, the bed has a hump, and the dam separates two different water levels exactly at the tip of the hump. Due to the complex nature of the problem, numerical instability and dissipation can arise, as reported in Hudson (1999). The flow domain is a 1 m long rectangular channel with reflective boundaries at $x = 0$ m and $x = 1$ m. The variable bed topography is defined as

$$z(x) = \begin{cases} \frac{1}{8}(\cos(10\pi(x - 0.5)) + 1) & \text{if } \frac{2}{5} \leq x \leq \frac{3}{5} \\ 0 & \text{otherwise} \end{cases}$$

Table 4 | Norm of non-dimensional error $L_2(h)$ and $L_2(u)$ for the dam-break on the wet bed

Points N	Without limiter		With limiter	
	$L_2(h)$	$L_2(u)$	$L_2(h)$	$L_2(u)$
80	3.89×10^{-2}	3.97×10^{-2}	2.26×10^{-2}	2.45×10^{-2}
150	3.55×10^{-2}	3.26×10^{-2}	1.59×10^{-2}	1.52×10^{-2}
300	2.14×10^{-2}	2.11×10^{-2}	9.41×10^{-3}	9.43×10^{-3}
600	1.41×10^{-2}	1.38×10^{-2}	6.05×10^{-3}	5.82×10^{-3}

Table 5 | Root mean square errors h_{RMSE} and Q_{RMSE} for dam-break on the dry bed

Points N	Without limiter		With limiter	
	h_{RMSE}	Q_{RMSE}	h_{RMSE}	Q_{RMSE}
80	2.409×10^{-1}	2.467×10	1.181×10^{-1}	1.217×10
150	1.804×10^{-1}	1.561×10	7.636×10^{-2}	5.199×10^{-1}
300	1.092×10^{-1}	1.113×10	3.113×10^{-2}	3.017×10^{-1}
600	6.842×10^{-2}	7.171×10^{-1}	1.451×10^{-2}	1.279×10^{-1}

The dam is placed at $x = 0.5$ m, which separates the channel into two initial water columns. The initial conditions are defined as

$$Q(x, 0) = 0 \quad \text{and} \quad h(x, 0) = \begin{cases} 1 - z(x) & \text{if } 0 \leq x \leq \frac{1}{2} \\ \frac{1}{2} - z(x) & \text{if } \frac{1}{2} \leq x \leq 1 \end{cases}$$

Here, the domain is distributed with 1,000 irregular points, and the time step is taken as $\Delta t = 0.0001$. At the time $t = 0$ s, the dam is removed instantaneously, and results are noted at $t = 0.1$ s after the removal of the dam. The computed water surface profile and discharge along the channel are compared with the analytical solutions by Hubbard's approach in Figure 9. The analytical solution is discussed in Hudson (1999). It is very interesting to observe that the proposed meshless method can accurately capture the transition in flow depth and velocity.

Steady flow over a hump

A series of tests were performed in the workshop on dam-break wave simulations by Goutal & Maurel (1997) to evaluate the ability of numerical schemes to represent the critical transitions correctly and to validate the treatment of source terms as it involves spatially varying bottom topography. Also, these tests were widely used to study the convergence of numerical solutions. Also, the problems are selected so that flow regimes can be subcritical, supercritical, or transcritical. The channel is considered to be 25 m long with a hump defined by

$$z(x) = \begin{cases} 0, & \text{for } x \leq 8 \text{ m} \\ 0.2 - 0.05(x - 10)^2, & \text{for } 8 < x < 12 \text{ m} \\ 0, & \text{for } x \geq 12 \text{ m} \end{cases}$$

Depending on the initial and boundary conditions, the flow may be subcritical, transcritical with shock or without shock, or supercritical. For all the cases presented below, the domain is represented by 233 irregularly distributed points. The time step, $\Delta t = 0.01$ s, is used for a stable solution. Three different flow conditions are simulated and presented below.

Subcritical flow

For this test, a discharge per unit width of $q = 4.42$ m²/s and the constant water surface level of 2 m are set as upstream and downstream boundary conditions, respectively. The simulation is continued for a sufficiently long time to achieve the steady-state condition. The results are plotted in Figure 10 and show a good agreement between numerical and analytical solutions. The discharge at the point of bed transition downstream is deviated by 0.18%. However, such a deviation is insignificant compared with previous studies (e.g., Valiani & Begnudelli 2006).

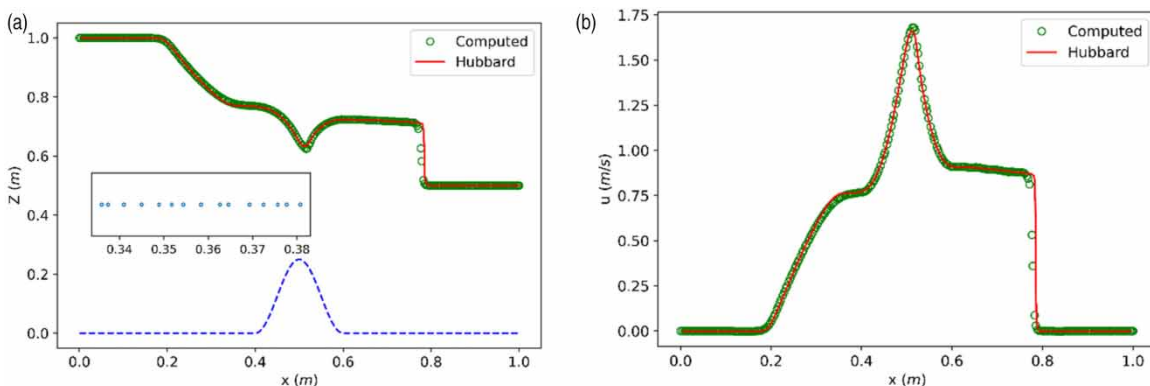


Figure 9 | Dam break on a variable depth riverbed: (a) water surface elevation and (b) velocity.

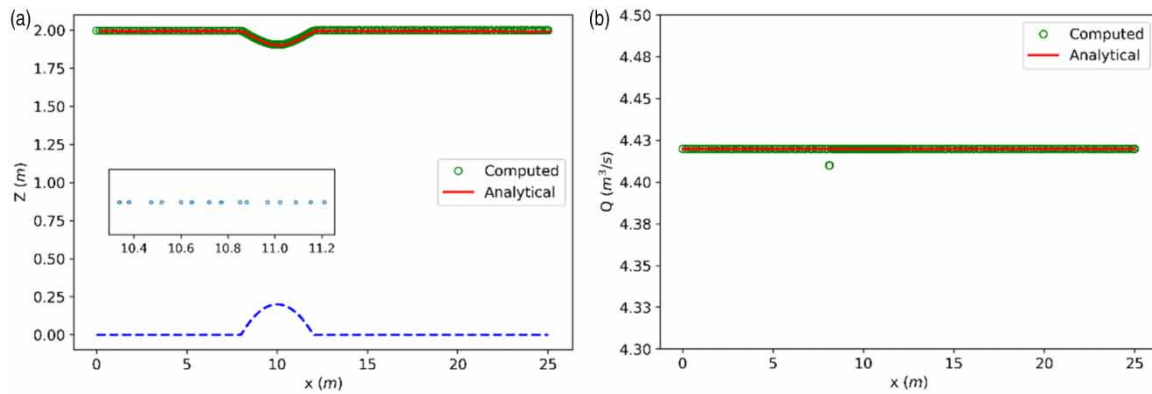


Figure 10 | Subcritical flow over a hump: (a) water surface elevation and (b) discharge.

Transcritical flow without a shock

For this test, the upstream inflow discharge per unit width of $q = 1.53 \text{ m}^2/\text{s}$ is imposed, and at the downstream, no boundary condition is needed since the flow is supercritical. Figure 11 compares the numerical and analytical solutions at the steady state. In this case, there is no deviation in discharge that can be observed.

Transcritical flow with a shock

For this test, the upstream inflow discharge per unit width of $q = 0.18 \text{ m}^2/\text{s}$ and a constant water surface elevation of 0.33 m are set as upstream and downstream boundary conditions, respectively. Figure 12 shows the comparison of numerical and

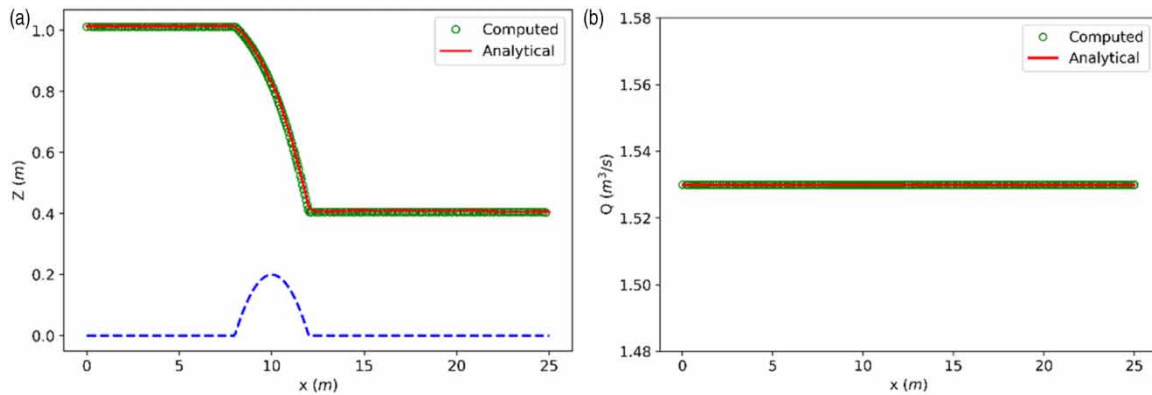


Figure 11 | Transcritical flow without a shock: (a) water surface elevation and (b) discharge.

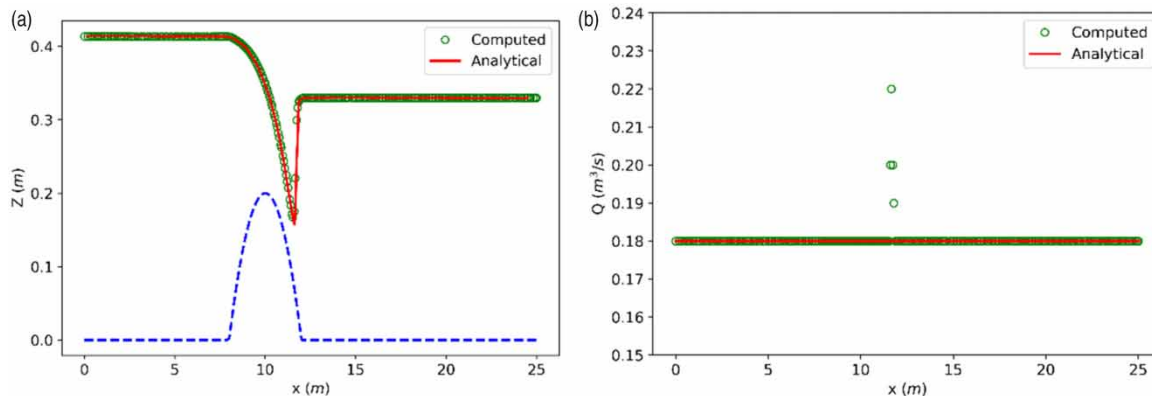


Figure 12 | Transcritical flow with a shock: (a) water surface elevation and (b) discharge.

analytical solutions of water surface elevation and unit discharge along the channel at the steady state. The discharge at the point of bed transition at downstream is deviated by 14.83%. Similar differences were reported as 10% by Zhou *et al.* (2002), 23% by Valiani & Begnudelli (2006), and 15% by Brufau *et al.* (2002). It is worth stressing that an error on the discharge does not imply errors in mass conservation (Valiani & Begnudelli 2006), and hence the behavior of the system may still be considered very good.

It can be concluded from the above set of tests that the proposed meshless method can successfully simulate different flow regimes in the presence of bed variation and shocks. It should also be noted that the results obtained from the meshless method are superior compared with many previous studies based on the FVM and approximate Riemann solvers.

Tidal wave flow over a step

This test problem was proposed by the EU CADAM project and investigated later by Zhou *et al.* (2002). A tidal wave propagates in a frictionless 1,500 m long channel with two vertical steps. The bed topography is defined as

$$z(x) = \begin{cases} 8 & \text{if } |x - 750| \leq 187.5 \\ 0 & \text{otherwise} \end{cases}$$

An asymptotic analytical solution is given by Bermudez & Vazquez (1994) as

$$Z(x, t) = 20 - 4 \sin\left(\pi\left(\frac{4t}{86,400} + \frac{1}{2}\right)\right)$$

$$u(x, t) = \frac{(x-L)\pi}{5400h(x, t)} \cos\left(\pi\left(\frac{4t}{86,400} + \frac{1}{2}\right)\right)$$

However, the presence of vertical steps makes numerical computation difficult. The sharp discontinuity in the bed topography can often result in numerical instability. The computations use 200 points distributed irregularly along the channel. Numerical results are compared at $t = 10,800$ s with the analytical solutions in Figure 13. It can be observed from the comparison that the proposed meshless method can accurately capture the flow discontinuity due to the presence of vertical steps on the bed.

Hydraulic jump in a divergent channel

This experimental test aims to check the ability of the scheme to deal with nonprismatic effects due to channel width variation and discontinuous flow simultaneously. The experimental test for a hydraulic jump in a divergent channel was conducted by Khalifa (1981). The numerical simulations were carried out by Younus & Chaudhry (1994) and Capart *et al.* (2003) for the same experimental observation to test a 2D shallow water solver. In this test, the channel length is 2.5 m with rectangular cross-sections. However, the channel width varies, as shown in Figure 14, following the below

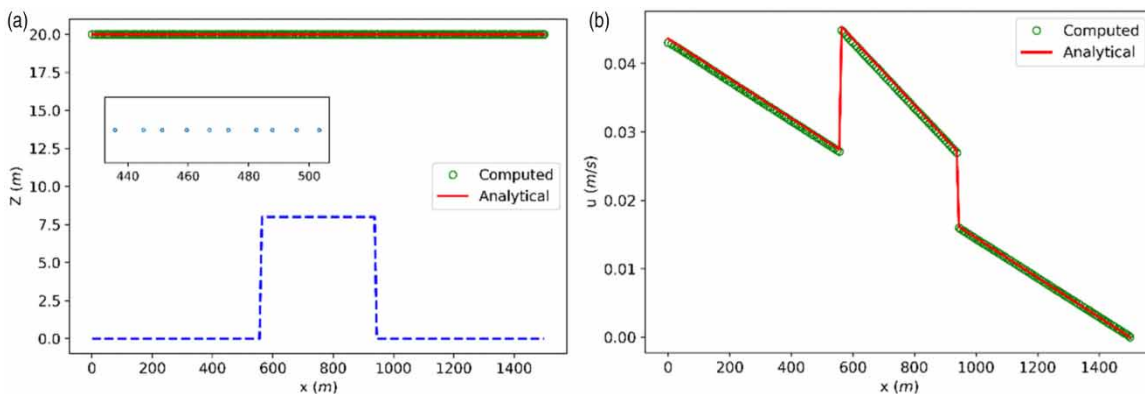


Figure 13 | Tidal wave over a step: (a) water surface elevation and (b) velocity.

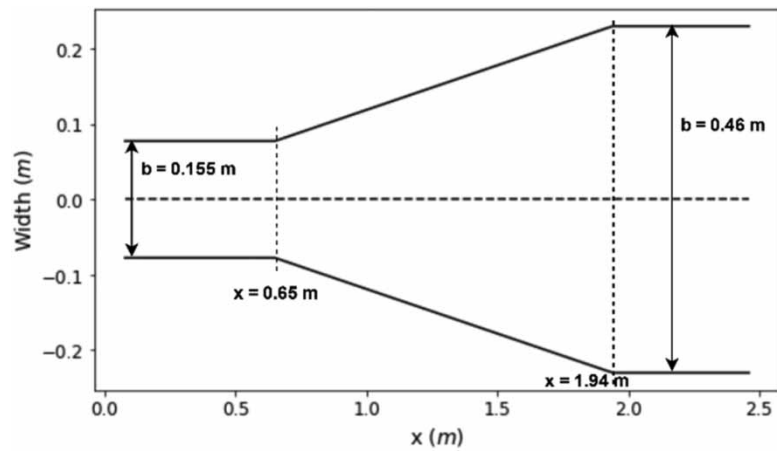


Figure 14 | Hydraulic jump in a rectangular channel: diverging channel width variation.

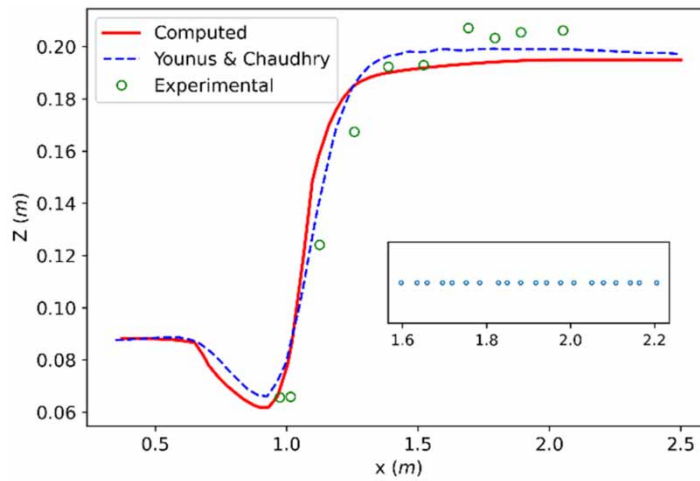


Figure 15 | Hydraulic jump in a diverging channel.

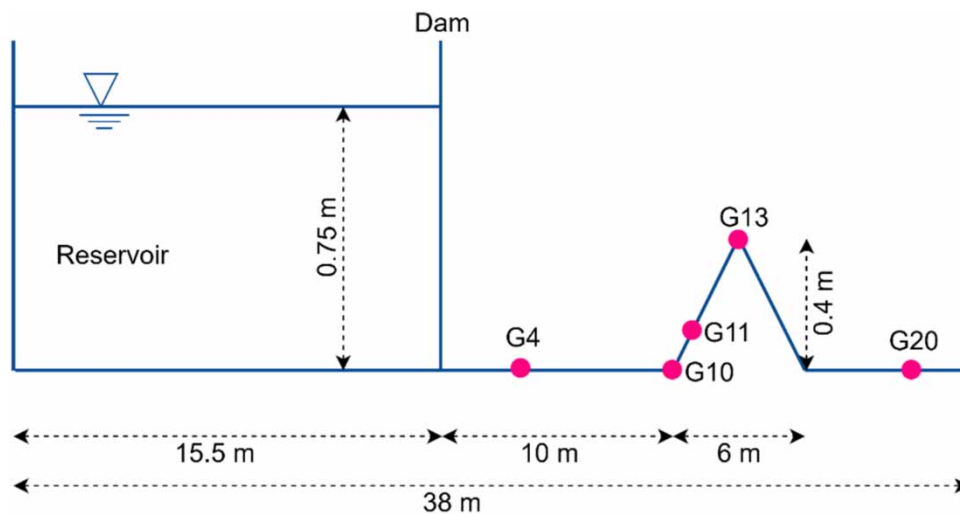


Figure 16 | Geometry and gauge locations in the experimental and model setup.

expression:

$$B(x) = \begin{cases} 0.155 \text{ m}, & x \leq 0.65 \text{ m} \\ 0.155 + \left(\frac{0.305}{1.29}\right)(x - 0.65) \text{ m}, & 0.65 \text{ m} < x \leq 1.94 \text{ m} \\ 0.46 \text{ m}, & x > 1.94 \text{ m} \end{cases}$$

The channel geometry is described by 80 points distributed irregularly along the length. At the upstream boundary, water depth of 0.088 m and discharge of 0.0263 m³/s at the inlet, and a water depth of 0.195 m at the outlet are prescribed as

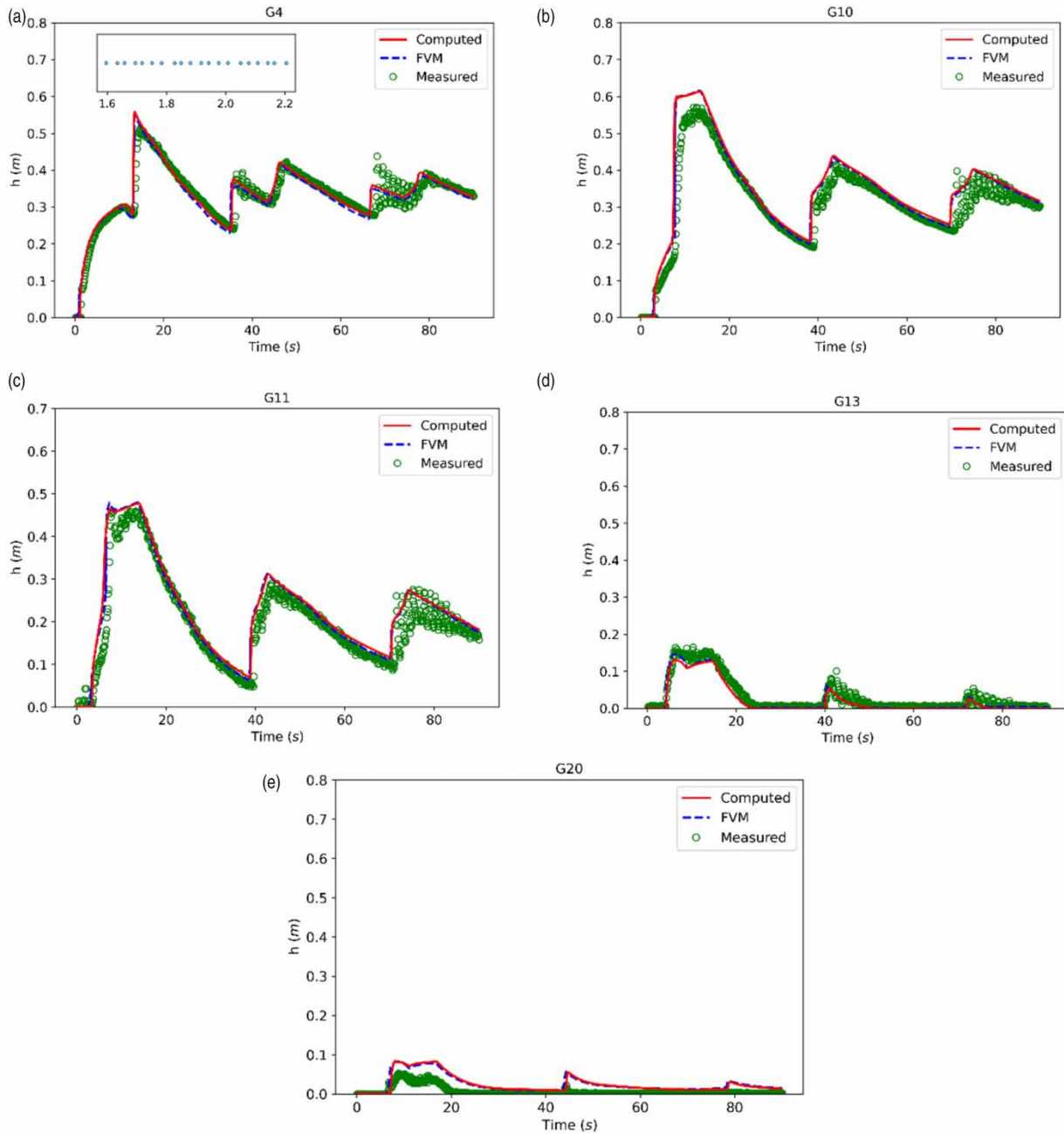


Figure 17 | Computed and measured water depth variations at different stations: (a) G4, (b) G10, (c) G11, (d) G13, and (e) G20.

boundary conditions. At steady state, a hydraulic jump is formed as shown in Figure 15. The proposed numerical scheme can accurately capture the location and profile of the hydraulic jump as compared with the experimental observation in Figure 15. The present numerical solution is also compared with the 2D model results of Younus & Chaudhry (1994) and no significant differences are observed.

Flow over a triangular obstacle

This experimental test is carried out to reproduce the laboratory dam-break flow over a triangular hump recommended by the EU CADAM project. The physical experiment included complex hydraulic properties such as shocks, transitions between wet and dry beds, and flow over an obstacle. The laboratory setup is illustrated in Figure 16. The experiment consisted of a reservoir with water up to 0.75 m contained by a dam located at $x = 55.5$ m and a dry bed downstream within a rectangular channel. A symmetric triangular obstacle (6 m long and 0.4 m high) was placed on the channel, with its peak located 13 m downstream of the dam. To observe depth evolution, gauges were located at 4 m (G4), 10 m (G10), 11 m (G11), 13 m (G13), and 20 m (G20) from the dam as shown in Figure 16. The gauge point G13 was located at the vertex of the obstacle, and therefore it is a critical point. The fixed boundaries are walls except for the open outlet. The Manning's roughness coefficient was supplied as $0.0125 \text{ m}^{-1/3} \text{ s}$ by the experimentalists (Brufau *et al.* 2002).

In the computation, 380 points are distributed irregularly along the channel. The time step, $\Delta t = 0.001$ s, and a dry bed tolerance, $h_{tol} = 0.0001$ m, are used. The simulation is carried out for 90 s. The depth variation with respect to time at the five gauges is compared with the experimental observations in Figure 17. It can be seen that the simulated flow depths closely follow the observed data with respect to depth variation and arrival time of the waterfront to the respective gauges. The transition from wet to dry and vice versa at the gauge point G13 is also well predicted. The flow depth comparison at the tip of the hump shows that the proposed meshless method has better agreement with the experimental measurement than the FVM-based solution reported by Kuiry *et al.* (2012). However, similar to earlier studies by Chaabelasri *et al.* (2019), a large deviation with respect to experimental data can be seen at G20, but the flow depth variation at this location during the entire simulation period is very small.

CONCLUSIONS

A meshless shock-capturing method is presented for solving the 1D Saint-Venant equations describing open channel flow. The HLL approximate Riemann solver is implemented within the framework of the WLS method for capturing shocks and flow discontinuity. The first-order Euler time discretization results in similar level of accuracy to that of the second-order Runge–Kutta time discretization method but in significantly less computation time. A stability condition for the proposed explicit scheme is shown to produce convergent solutions. The paper describes the theoretical background, verification, and validation of the 1D shock-capturing meshless method for solving the Saint-Venant equations. The robustness of the proposed meshless method is verified by comparing the simulated results with several theoretical benchmark tests and laboratory experiments. The presented method is stable and does not artificially accelerate while solving still-water conditions in a closed domain. The predictions of the water surface elevation and discharge for an ideal dam break on the wet and dry bed are in very good agreement with the analytical solutions. The flow discontinuity over vertical steps is accurately captured by the developed method. The hydraulic jump formed in a laboratory scale divergent channel is reproduced with a similar accuracy level to a previous study. The water wave propagation due to a dam break on a dry bed over a triangular obstacle is well simulated, and the computed results closely follow the experimental observations. Also, the shifting of dry and wet conditions is well captured. The meshless method presented in this study can be extended to solve the 2D shallow water equations to capture sharp changes in topography and flow dynamics by distributing a greater number of localized points.

ACKNOWLEDGEMENTS

This research is financially supported by the Indian Institute of Technology Madras under the MHRD project (Project No. SB20210848MAMHRD008558).

DATA AVAILABILITY STATEMENT

All relevant data are included in the paper or its Supplementary Information.

CONFLICT OF INTEREST

The authors declare there is no conflict.

REFERENCES

- Belytschko, T., Lu, Y. Y., Gu, L. & Tabbara, M. 1995 Element-free Galerkin methods for static and dynamic fracture. *International Journal of Solids and Structures* **32** (17–18), 2547–2570.
- Bermudez, A. & Vazquez, M. E. 1994 Upwind methods for hyperbolic conservation laws with source terms. *Computers & Fluids* **23** (8), 1049–1071.
- Brufau, P., Vázquez-Cendón, M. E. & García-Navarro, P. 2002 A numerical model for the flooding and drying of irregular domains. *International Journal for Numerical Methods in Fluids* **39** (3), 247–275.
- Buachart, C., Kanok-Nukulchai, W., Ortega, E. & Onate, E. 2014 A shallow water model by finite point method. *International Journal of Computational Methods* **11** (1), 1350047.
- Capart, H., Eldho, T. I., Huang, S. Y., Young, D. L. & Zech, Y. 2003 Treatment of natural geometry in finite volume river flow computations. *Journal of Hydraulic Engineering* **129** (5), 385–393.
- Chaabelasri, E. 2018 Numerical simulation of dam break flows using a radial basis function meshless method with artificial viscosity. *Modelling and Simulation in Engineering* **2018**, 4245658.
- Chaabelasri, E., Jeyar, M. & Borthwick, A. G. 2019 Explicit radial basis function collocation method for computing shallow water flows. *Procedia Computer Science* **148**, 361–370.
- Chang, T. J., Kao, H. M., Chang, K. H. & Hsu, M. H. 2011 Numerical simulation of shallow-water dam break flows in open channels using smoothed particle hydrodynamics. *Journal of Hydrology* **408** (1–2), 78–90.
- Chen, H. Q. & Shu, C. 2005 An efficient implicit mesh-free method to solve two-dimensional compressible Euler equations. *International Journal of Modern Physics C* **16** (03), 439–454.
- Eymard, R., Gallouët, T. & Herbin, R. 2000 Finite volume methods. In: *Handbook of Numerical Analysis*. Vol. 7, (P. G. Ciarlet & J. L. Lions, eds.). Elsevier, Amsterdam, The Netherlands, pp. 713–1018.
- Fazli Malidareh, B., Abbas Hosseini, S. & Jabbari, E. 2016 Discrete mixed subdomain least squares (DMSLS) meshless method with collocation points for modeling dam-break induced flows. *Journal of Hydroinformatics* **18** (4), 702–723.
- Fennema, R. J. & Chaudhry, M. H. 1990 Explicit methods for 2-D transient free surface flows. *Journal of Hydraulic Engineering* **116** (8), 1013–1034.
- George, D. 2008 Augmented Riemann solvers for the shallow water equation over variable topography with steady state and inundation. *Journal of Computational Physics* **227** (6), 3089–3113.
- Ghostine, R., Hoteit, I., Vazquez, J., Terfous, A., Ghenaïm, A. & Mose, R. 2015 Comparison between a coupled 1D-2D model and a fully 2D model for supercritical flow simulation in crossroads. *Journal of Hydraulic Research* **53** (2), 274–281.
- Gingold, R. A. & Monaghan, J. J. 1977 Smoothed particle hydrodynamics: theory and application to non-spherical stars. *Monthly Notices of the Royal Astronomical Society* **181** (3), 375–389.
- Goutal, N. & Maurel, F. 1997 Electricité de France Service Applications de l'Electricité et Environnement & Workshop on Dam-Break Wave Simulation. In: *Proceedings of the 2nd Workshop on Dam-Break Wave Simulation* (N. Goutal, ed.). Direction des études et recherches, Electricité de France, Paris.
- Haleem, D. A., Kesserwani, G. & Caviedes-Voullième, D. 2015 Haar wavelet-based adaptive finite volume shallow water solver. *Journal of Hydroinformatics* **17** (6), 857–873.
- Harten, A., Lax, P. D. & Leer, B. V. 1983 On upstream differencing and Godunov-type schemes for hyperbolic conservation laws. *SIAM Review* **25** (1), 35–61.
- Hudson, J. 1999 *Numerical Techniques for the Shallow Water Equations, Numerical Analysis Report 2/99*. University of Reading (A colour postscript version of this report can be obtained at. Available from: <http://www.rdg.ac.uk/AcaDepts/sm/home.html>).
- Jefferies, A., Kuhnert, J., Aschenbrenner, L. & Giffhorn, U. 2015 Finite pointset method for the simulation of a vehicle travelling through a body of water. In: *Meshfree Methods for Partial Differential Equations VII*. (M. Griebel & M. A. Schweitzer, eds.) Springer, Cham, pp. 205–221.
- Khalifa, A. 1981 *Theoretical and Experimental Study of the Radial Hydraulic Jump: A Dissertation*. University of Windsor.
- Kuhnert, J. 2003 An upwind finite pointset method (FPM) for compressible Euler and Navier–Stokes equations. In: *Meshfree Methods for Partial Differential Equations* (M. Griebel & M. A. Schweitzer, eds.). Springer, Berlin, Heidelberg, pp. 239–249.
- Kuhnert, J. & Ostermann, I. 2014 The finite pointset method (FPM) and an application in soil mechanics. In: *Mathematics of Planet Earth* (E. Pardo-Igúzquiza, C. Guardiola-Albert, J. Heredia, Luis Moreno-Merino, J. J. Durán & J. A. Vargas-Guzmán, eds.). Springer, Berlin, Heidelberg, pp. 815–818.
- Kuiry, S. N., Pramanik, K. & Sen, D. 2008 Finite volume model for shallow water equations with improved treatment of source terms. *Journal of Hydraulic Engineering* **134** (2), 231.
- Kuiry, S. N., Wu, W. & Ding, Y. 2012 A one-dimensional shock-capturing model for long wave run-up on sloping beaches. *ISH Journal of Hydraulic Engineering* **18** (2), 65–79.
- LeVeque, R. J. 2002 *Finite Volume Methods for Hyperbolic Problems*. Cambridge University Press, Cambridge, UK.

- Li, P.-W. & Fan, L.-M. 2017 Generalized finite difference method for two-dimensional shallow water equations. *Engineering Analysis with Boundary Elements* **80**, 58–71.
- Liang, S. J., Tang, J. H. & Wu, M. S. 2008 Solution of shallow-water equations using least-squares finite-element method. *Acta Mechanica Sinica* **24** (5), 523–532.
- Ma, Z., Chen, H. & Zhou, C. 2008 A study of point moving adaptivity in gridless method. *Computer Methods in Applied Mechanics and Engineering* **197** (21–24), 1926–1937.
- Moller, A. & Kuhnert, J. 2007 Simulation of the glass flow inside a floating process/Simulation de l'écoulement du verre dans le procede float. *VERRE-PARIS THEN VERSAILLES-* **13** (5), 28.
- Molls, T. & Chaudhry, M. H. 1995 Depth-averaged open-channel flow model. *Journal of Hydraulic Engineering* **121** (6), 453–465.
- Monaghan, J. J. 1992 Smoothed particle hydrodynamics. *Annual Review of Astronomy and Astrophysics* **30**, 543–574.
- Nayroles, B., Touzot, G. & Villon, P. 1992 Generalizing the finite element method: diffuse approximation and diffuse elements. *Computational Mechanics* **10** (5), 307–318.
- Rogers, B. D., Borthwick, A. G. & Taylor, P. H. 2003 Mathematical balancing of flux gradient and source terms prior to using Roe's approximate Riemann solver. *Journal of Computational Physics* **192** (2), 422–451.
- Suchde, P., Kuhnert, J., Schröder, S. & Klar, A. 2017 A flux conserving meshfree method for conservation laws. *International Journal for Numerical Methods in Engineering* **112** (3), 238–256.
- Tiwari, S. & Kuhnert, J. 2002 A meshfree method for incompressible fluid flows with incorporated surface tension. *Revue européenne des éléments finis* **11** (7–8), 965–987.
- Tiwari, S. & Kuhnert, J. 2003a Finite pointset method based on the projection method for simulations of the incompressible Navier–Stokes equations. In: *Meshfree Methods for Partial Differential Equations* (M. Griebel & M. A. Schweitzer, eds.). Springer, Berlin, Heidelberg, pp. 373–387.
- Tiwari, S. & Kuhnert, J. 2003b Particle method for simulation of free surface flows. In: *Hyperbolic Problems: Theory, Numerics, Applications* (T. Y. Hou & E. Tadmor, eds.). Springer, Berlin, Heidelberg, pp. 889–898.
- Tiwari, S. & Kuhnert, J. 2007 Modeling of two-phase flows with surface tension by finite pointset method (FPM). *Journal of Computational and Applied Mathematics* **203** (2), 376–386.
- Tiwari, S., Antonov, S., Hietel, D., Kuhnert, J., Olawsky, F. & Wegener, R. 2007 A meshfree method for simulations of interactions between fluids and flexible structures. In: *Meshfree Methods for Partial Differential Equations III* (M. Griebel & M. A. Schweitzer, eds.). Springer, Berlin, Heidelberg, pp. 249–264.
- Toro, E. F. 2001 *Shock-Capturing Methods for Free-Surface Shallow Flows*. John Wiley & Sons, Chichester, UK.
- Tramecon, A. & Kuhnert, J. 2013 *Simulation of Advanced Folded Airbags with VPS-PAMCRASH/FPM: Development and Validation of Turbulent Flow Numerical Simulation Techniques Applied to Curtain Bag Deployments (No. 2013-01-1158)*. SAE Technical Paper. 2013-01-1158. <https://doi.org/10.4271/2013-01-1158>.
- Uhlmann, E., Gerstenberger, R. & Kuhnert, J. 2013 Cutting simulation with the meshfree finite pointset method. *Procedia Cirp* **8**, 391–396.
- Vaccondio, R., Rogers, B. D. & Stansby, P. K. 2012a Accurate particle splitting for SPH in shallow water with shock capturing. *International Journal for Numerical Methods in Fluids* **69** (8), 1377–1410.
- Vaccondio, R., Rogers, B. D., Stansby, P. K. & Mignosa, P. 2012b SPH Modeling of Shallow Flow with Open Boundaries for Practical Flood Simulation. *Journal of Hydraulic Engineering* **138** (6), 530–541.
- Vaccondio, R., Rogers, B. D., Stansby, P. K. & Mignosa, P. 2013 A correction for balancing discontinuous bed slopes in two-dimensional smoothed particle hydrodynamics shallow water modeling. *International Journal for Numerical Methods in Fluids* **71** (7), 850–872.
- Valiani, A. & Begnudelli, L. 2006 Divergence form for bed slope source term in shallow water equations. *Journal of Hydraulic Engineering* **132** (7), 652–665.
- Wang, Z. & Shen, H. T. 1999 Lagrangian simulation of one-dimensional dam-break flow. *Journal of Hydraulic Engineering* **125** (11), 1217–1220.
- Ying, X. & Wang, S. S. 2008 Improved implementation of the HLL approximate Riemann solver for one-dimensional open channel flows. *Journal of Hydraulic Research* **46** (1), 21–34.
- Ying, X., Khan, A. A. & Wang, S. S. 2004 Upwind conservative scheme for the Saint Venant equations. *Journal of Hydraulic Engineering* **130** (10), 977–987.
- Yoon, T. H. & Kang, S. K. 2004 Finite volume model for two-dimensional shallow water flows on unstructured grids. *Journal of Hydraulic Engineering* **130** (7), 678–688.
- Younus, M. & Hanif Chaudhry, M. 1994 A depth-averaged turbulence model for the computation of free-surface flow. *Journal of Hydraulic Research* **32** (3), 415–444.
- Zhou, J. G., Causon, D. M., Mingham, C. G. & Ingram, D. M. 2001 The surface gradient method for the treatment of source terms in the shallow-water equations. *Journal of Computational Physics* **168** (1), 1–25.
- Zhou, J. G., Causon, D. M., Ingram, D. M. & Mingham, C. G. 2002 Numerical solutions of the shallow water equations with discontinuous bed topography. *International Journal for Numerical Methods in Fluids* **38** (8), 769–788.

First received 2 October 2022; accepted in revised form 3 June 2023. Available online 19 June 2023